Phaseless Passive Synthetic Aperture Imaging with Regularized Wirtinger Flow

K. Aditi*, A. Anil Kumar*, Angshul Majumdar†, Tapas Chakravarty*, Kriti Kumar*

*TCS Research, Bangalore, India, †IIIT-Delhi, New Delhi, India
{aditi.k6, achannaanil.kumar, tapas.chakravarty, kriti.kumar}@tcs.com, angshul@iiitd.ac.in

Abstract—In this paper, we present a training-less methodology for Phaseless Passive Synthetic Aperture Radar imaging. The existing approach based on Wirtinger Flow (WF) requires large number of phaseless measurements for satisfactory reconstruction. To address this issue, we propose a regularized Wirtinger Flow based approach that helps with efficient image reconstruction. We employ Total Variation, BM3D and Deep Image Prior based regularizers/denoisers in an ADMM framework for the proposed solution. The results indicate that compared to the state-of-the-art, the proposed approach not only facilitates better reconstruction with lesser measurements but also shows robustness against SAR trajectory errors.

Index Terms—Passive SAR, Wirtinger Flow, phase retrieval, regularization, ADMM, Denoiser.

I. Introduction

Synthetic Aperture Radar (SAR) imaging is an all weather friendly imaging paradigm that has numerous applications [1]– [3]. Among several SAR imaging modalities, the passive SAR imaging modality which uses signals of opportunity is gaining lot of attention these days. The key advantages of employing such passive SAR systems are reduction in cost, moderate hardware requirement and less burden on already crowded electromagnetic spectrum [4]. Classically, passive SAR is achieved by using interferometric technique with multiple receivers [5], [6]. However, these multiple receivers must be properly synchronized to avoid imaging errors. To overcome this issue of synchronization, lately a new passive SAR imaging paradigm referred to as Phaseless Passive SAR (PPSAR) imaging is becoming popular, as it uses only a single receiver. In this paper, we consider this emerging PPSAR imaging paradigm and propose a training-less method for improved imaging.

While PPSAR is an attractive paradigm, standard SAR reconstruction algorithms are not directly applicable due to the phaseless measurements. Till date, limited literature exists on PPSAR image reconstruction [7], [8], [9]. A Low Rank Matrix Recovery (LRMR) based approach using *lifting* was proposed in [7]. The major drawback of this approach is that the lifting operation increases the dimension of the unknown image space, making it computationally demanding and memory intensive. These limitations make LRMR to scale poorly and restrict the dimension of the image that can be reconstructed. The use Wirtinger Flow [10] as the recovery algorithm was proposed in [8]. Unlike LRMR approach, Wirtinger Flow does not alter the dimension of the problem and uses gradient descent for optimization. Throughout this paper, we will refer the approach in [8] as the vanilla Wirtinger Flow (vWF). The vWF provides better reconstruction with reduced computational complexity compared to LRMR approach [8]. However, it requires large number of measurements for satisfactory reconstruction. In SAR systems, this leads to provisioning of more on-board storage and/or a high speed data link between the mobile platform and the ground station. These requirements are undesirable in practice as SAR systems are deployed on resource constrained platforms.

A possible way to overcome the aforementioned problem is to have better algorithms that use suitable regularizers which facilitate reconstruction with fewer measurements. More recently, a Wirtinger Flow based approach imposing regularization with Generative Prior (GP) was proposed in [9]. However, the improvement in performance is at the expense of the training data requirements.

On the contrary, in this paper we address the PPSAR image reconstruction with the Wirtinger Flow based approach in a *training-less* setting, that is, we do not train any network that learns to recover the unknown SAR image. Towards this goal, our contributions are as follows. Firstly, we propose a regularized Wirtinger Flow (rWF) based formulation that uses suitable regularizers to facilitate image reconstruction with fewer measurements. Secondly, while one can use a solution similar to [11], here we use the Alternating Direction Method of Multipliers (ADMM) [12] as it has been shown to be highly efficient for non-convex problems [13], [14]. The ADMM approach helps in application of various denoisers in a Plug-and-play (PnP) manner [15]. Thirdly, we employ standard denoisers such as Total Variation [16] and BM3D [17]. Further, we also apply the Deep Image Prior [18] for denoising where early stopping works as regularization. We demonstrate the effectiveness of the aforementioned denoisers for the PPSAR problem. In general, the results demonstrate the superior performance of the proposed rWF approach in giving good reconstruction. In particular, rWF with Total Variation provides 75% reduction in measurements compared to the state-of-the-art [8]. In addition, rWF is also more robust to SAR trajectory errors when compared with vWF.

The rest of the paper is organized as follows. Section II provides a brief description of the PPSAR signal model. Subsequently, Section III describes the proposed approach in detail. The performance comparison of the proposed approach

with that of vWF is provided in Section IV. Finally, Section V concludes the paper.

II. PHASELESS PASSIVE SAR SIGNAL MODEL

In this paper, we use an identical PPSAR signal model as that of [8] and also provide a brief description for the sake of continuity. We assume a single mobile receiver moving over the scene of interest whose trajectory is given by $\boldsymbol{\gamma}(s) \in \mathbb{R}^3$, '$s$' represents the slow-time index, which is sampled at suitable measurement intervals. Let $\boldsymbol{X} = (\boldsymbol{x}, \psi(\boldsymbol{x})) \in \mathbb{R}^3$ denote the earth's surface with $\boldsymbol{x} = (x_1, x_2)$ and $\psi(\boldsymbol{x})$ is the ground topography which is assumed to be known. The ground reflectivity at any ground location $\boldsymbol{x}$ is denoted by $\rho(\boldsymbol{x})$ and $\mathbf{y}$ represents the location of the fixed transmitter.

Under the start-stop and Born scattering approximations, the fast-time Fourier transform of the received signal can be expressed as [5]:

$$f(\omega, s) = \int e^{-i\omega\phi(s, \boldsymbol{x}, \mathbf{y})/c} A(\omega, s, \boldsymbol{x})\rho(\boldsymbol{x})d\boldsymbol{x}, \quad (1)$$

where $\phi(s, \boldsymbol{x}, \mathbf{y}) = |\mathbf{y} - \boldsymbol{x}| + |\boldsymbol{x} - \boldsymbol{\gamma}(s)|$, $A(\omega, s, \boldsymbol{x})$ (see [8, eq. 3]) is the amplitude function which depends upon the transmit and receive antenna beam pattern, and for the spotlight SAR configuration $A(\omega, s, \boldsymbol{x}) \approx 1$ and ω is the frequency index. Upon autocorrelation of the fast-time samples and using the autocorrelation property in the frequency domain, the measurements are given as:

$$d(\omega, s) = f(\omega, s)^* f(\omega, s) = |f(\omega, s)|^2, \quad (2)$$

where $(.)^*$ denotes the complex conjugate. Please note that due to $|.|^2$, the measurements become phaseless. By substituting (1) into (2), $d(\omega, s)$ can be expressed as:

$$d(\omega, s) = \int\int \rho(\boldsymbol{x})\rho(\tilde{\boldsymbol{x}})e^{-i\omega\xi(s, \boldsymbol{x}, \tilde{\boldsymbol{x}}, \mathbf{y})/c}d\boldsymbol{x}d\tilde{\boldsymbol{x}}, \quad (3)$$

where $\xi(s, \boldsymbol{x}, \tilde{\boldsymbol{x}}, \mathbf{y}) = |\mathbf{y} - \boldsymbol{x}| + |\boldsymbol{x} - \boldsymbol{\gamma}(s)| - |\mathbf{y} - \tilde{\boldsymbol{x}}| - |\tilde{\boldsymbol{x}} - \boldsymbol{\gamma}(s)|$. With far-field and small scene assumptions, $|\mathbf{y} - \boldsymbol{x}| - |\mathbf{y} - \tilde{\boldsymbol{x}}| \approx \hat{\mathbf{y}} \cdot (\tilde{\boldsymbol{x}} - \boldsymbol{x})$ (see [19, Appendix A]), where $\hat{\mathbf{y}}$ is the unit vector of $\mathbf{y}$. Using the above approximations, the integrals in (3) can be separated and given as:

$$d(\omega, s) = \int \rho(\boldsymbol{x})e^{-i\omega(|\boldsymbol{x} - \boldsymbol{\gamma}(s)| - \hat{\mathbf{y}} \cdot \boldsymbol{x})/c}d\boldsymbol{x}$$
$$\times \int \rho(\tilde{\boldsymbol{x}})e^{i\omega(|\tilde{\boldsymbol{x}} - \boldsymbol{\gamma}(s)| - \hat{\mathbf{y}} \cdot \tilde{\boldsymbol{x}})/c}d\tilde{\boldsymbol{x}}. \quad (4)$$

Thus, one can observe that $d(\omega, s)$ depends only on the unit vector $\hat{\mathbf{y}}$ and not on the transmitter location $\mathbf{y}$. By discretizing the imaging scene into N small cells and discretizing (ω, s) with the appropriate sampling frequency and measurement intervals, the mth sampled measurement d_m corresponding to $(\omega, s)_m$, $m = 1, 2, ..., M$ can now be expressed as:

$$d_m = |\mathbf{L}_m^H \boldsymbol{\rho}|^2 = \mathbf{L}_m^H \boldsymbol{\rho}\boldsymbol{\rho}^H \mathbf{L}_m \quad (5)$$

where $\boldsymbol{\rho} \in \mathbb{R}^N$ and the nth element of $\boldsymbol{\rho}$, i.e., $\boldsymbol{\rho}_n = \boldsymbol{\rho}(\boldsymbol{x}_n)$ and $\mathbf{L}_m \in \mathbb{C}^N$, whose n^{th} element is given as:

$$[\mathbf{L}_m]^n = e^{-i\omega(|\boldsymbol{x}_n - \boldsymbol{\gamma}(s)| - \hat{\mathbf{y}} \cdot \boldsymbol{x}_n)/c}|_{(\omega, s)_m}. \quad (6)$$

Given $\boldsymbol{x}_n$ and $(\omega, s)_m$, $\mathbf{L}_m$ can be computed and thus, our task is now to estimate reflectivities $\boldsymbol{\rho}$ knowing the measurements d_m. As mentioned in Section I, one can either use the LRMR or vWF approach.

However, as shown in [8], vWF provides better performance compared to the LRMR approach without increasing the dimension but in general, requires more measurements for satisfactory reconstruction. In the following section, we describe the rWF based method which achieves good reconstruction with comparatively fewer number of measurements.

III. REGULARIZED WIRTINGER FLOW FOR PPSAR

We propose the following optimization problem to recover $\boldsymbol{\rho}$ from the measurements d_m

$$\widehat{\boldsymbol{\rho}} = \underset{\boldsymbol{\rho}}{\operatorname{argmin}} \mathcal{D}(\boldsymbol{\rho}) + \lambda\mathcal{R}(\boldsymbol{\rho}). \quad (7)$$

where $\mathcal{D}(\boldsymbol{\rho})$ is a data-fidelity term, $\mathcal{R}(\boldsymbol{\rho})$ represents the regularization term and the hyper-parameter λ controls the amount of regularization. For the data-fidelity term $\mathcal{D}(\boldsymbol{\rho})$, similar to [8], [10], we consider the simple quadratic loss function which is given as:

$$\mathcal{D}(\boldsymbol{\rho}) = \frac{1}{2M}\sum_{m=1}^{M}\left\|\mathbf{L}_m^H \boldsymbol{\rho}\boldsymbol{\rho}^H \mathbf{L}_m - d_m\right\|_2^2 \quad \text{(vWF)}. \quad (8)$$

The authors in [8] estimate $\boldsymbol{\rho}$ by minimizing only the above data-fidelity term without any regularization factor $\mathcal{R}(\boldsymbol{\rho})$. They solve it by using the gradient descent algorithm with Wirtinger derivatives as described in [10].

We solve (7) by using the variable splitting approach [20] for which we introduce proxy variable $\boldsymbol{v}$ and convert (7) into the following constrained optimization problem

$$\{\widehat{\boldsymbol{\rho}}, \widehat{\boldsymbol{v}}\} = \underset{\boldsymbol{\rho}, \boldsymbol{v}}{\operatorname{argmin}} \mathcal{D}(\boldsymbol{\rho}) + \lambda\mathcal{R}(\boldsymbol{v}) \quad \text{subject to} \quad \boldsymbol{\rho} = \boldsymbol{v}. \quad (9)$$

The Augmented Lagrangian corresponding to (9) can be expressed as [21], [22]:

$$\mathcal{L}(\boldsymbol{\rho}, \boldsymbol{v}, \boldsymbol{u}) = \mathcal{D}(\boldsymbol{\rho}) + \lambda\mathcal{R}(\boldsymbol{v}) + \boldsymbol{u}^T(\boldsymbol{\rho} - \boldsymbol{v}) + \frac{\mu}{2}\|\boldsymbol{\rho} - \boldsymbol{v}\|_2^2, \quad (10)$$

where μ is the penalty parameter and $\boldsymbol{u}$ represents the Lagrangian parameter. The minimizer of (9) is the saddle point of $\mathcal{L}(\boldsymbol{\rho}, \boldsymbol{v}, \boldsymbol{u})$ which can be found by solving (10) using the ADMM iterations that are given as [12], [23]:

$$\boldsymbol{\rho}^{(k+1)} = \underset{\boldsymbol{\rho}}{\operatorname{argmin}} \mathcal{D}(\boldsymbol{\rho}) + \frac{\mu}{2}\|\boldsymbol{\rho} - \tilde{\boldsymbol{\rho}}^{(k)}\|_2^2 \quad (11)$$

$$\boldsymbol{v}^{(k+1)} = \underset{\boldsymbol{v}}{\operatorname{argmin}} \frac{2\lambda}{\mu}\mathcal{R}(\boldsymbol{v}) + \|\boldsymbol{v} - \tilde{\boldsymbol{v}}^{(k)}\|_2^2 \quad (12)$$

$$\bar{\boldsymbol{u}}^{(k+1)} = \bar{\boldsymbol{u}}^{(k)} + (\boldsymbol{\rho}^{(k+1)} - \boldsymbol{v}^{(k+1)}) \quad (13)$$

where $\bar{\boldsymbol{u}}^{(k)} = \frac{1}{\mu}\boldsymbol{u}^{(k)}, \tilde{\boldsymbol{\rho}}^{(k)} = \boldsymbol{v}^{(k)} - \bar{\boldsymbol{u}}^{(k)}$ and $\tilde{\boldsymbol{v}}^{(k)} = \boldsymbol{\rho}^{(k+1)} + \bar{\boldsymbol{u}}^{(k)}$.

We solve the sub-problem (11) based on the Wirtinger derivatives. The initial estimate for the WF is important for its convergence and we choose the initial estimate $\boldsymbol{\rho}_0$ using the spectral method as described in [10]. The leading eigenvector

Algorithm 1 Algorithm for PPSAR

Require: $\{d^m\}_{m=1}^M$, $\{\mathbf{L^m}\}_{m=1}^M$, WF_iter, Total_iter, λ, μ, ϵ_1, ϵ_2.

  $\boldsymbol{\rho}_0 \leftarrow$ using Spectral Method
  $\boldsymbol{\rho}^{(0)} \leftarrow \boldsymbol{\rho}_0, \boldsymbol{v}^{(0)} \sim \mathcal{N}(0,1), \boldsymbol{u}^{(0)} \leftarrow \boldsymbol{\rho}^{(0)} - \boldsymbol{v}^{(0)}$
  $k \leftarrow 0, j \leftarrow 0$
  while $\frac{\|\boldsymbol{u}^{(k+1)} - \boldsymbol{u}^{(k)}\|}{\|\boldsymbol{u}^{(k)}\|} \leq \epsilon_1$ and $k < $ Total_iter **do**
    $\tilde{\boldsymbol{\rho}}^{(k)} \leftarrow \boldsymbol{v}^{(k)} - \boldsymbol{u}^{(k)}$
    $\boldsymbol{\rho}^{(0)} \leftarrow \boldsymbol{\rho}^{(k)}$
    while $\frac{\|\boldsymbol{\rho}^{(j+1)} - \boldsymbol{\rho}^{(j)}\|}{\|\boldsymbol{\rho}^{(j)}\|} \leq \epsilon_2$ and $j < $ WF_iter **do**
      $\boldsymbol{\rho}^{(j+1)} \leftarrow \boldsymbol{\rho}^{(j)} - \frac{\tau^{(j+1)}}{\|\boldsymbol{\rho}_0\|^2} \nabla \mathcal{J}\left(\boldsymbol{\rho}^{(j)}\right)$
      $j \leftarrow j + 1$
    end while
    $\boldsymbol{\rho}^{(k+1)} \leftarrow \boldsymbol{\rho}^{(j)}$
    $\tilde{\boldsymbol{v}}^{(k)} \leftarrow \boldsymbol{\rho}^{(k+1)} + \boldsymbol{u}^{(k)}$
    $\boldsymbol{v}^{(k+1)} \leftarrow$ prior update using rWF-TV/BM3D/DIP
    $\boldsymbol{u}^{(k+1)} \leftarrow \boldsymbol{u}^{(k)} + \boldsymbol{\rho}^{(k+1)} - \boldsymbol{v}^{(k+1)}$
    $k \leftarrow k + 1$
  end while
  return $\boldsymbol{\rho}^{(k+1)}$

---

of the positive semi-definite matrix $\mathbf{Y} = \sum_{m=1}^M d_m \mathbf{L}_m \mathbf{L}_m^H$ is chosen as the initial estimate [8]. The update step for $\boldsymbol{\rho}$ is given by:

$$\boldsymbol{\rho}^{(j+1)} = \boldsymbol{\rho}^{(j)} - \frac{\tau^{(j+1)}}{\|\boldsymbol{\rho}_0\|^2} \nabla \mathcal{J}(\boldsymbol{\rho}^{(j)}), \tag{14}$$

where $\mathcal{J}(\boldsymbol{\rho}^{(j)}) = \mathcal{D}(\boldsymbol{\rho}^{(j)}) + \frac{\mu}{2}\|\boldsymbol{\rho}^{(j)} - \tilde{\boldsymbol{\rho}}^{(k)}\|_2^2$ and its derivative is expressed as:

$$\nabla \mathcal{J}(\boldsymbol{\rho}^{(j)}) = \frac{1}{M} \sum_{m=1}^M \left(\mathbf{L}_m^H \boldsymbol{\rho}^{(j)} (\boldsymbol{\rho}^{(j)})^H \mathbf{L}_m - d_m\right) \mathbf{L}_m \mathbf{L}_m^H \boldsymbol{\rho}^{(j)}$$
$$+ \mu(\boldsymbol{\rho}^{(j)} - \tilde{\boldsymbol{\rho}}^{(k)}), \tag{15}$$

where $\tau^{(j)}$ denotes the step size at the jth update. The sub-problem (13) is a straightforward update step for $\boldsymbol{u}$.

The sub-problem (12) depends on the choice of prior and can also be viewed as a denoising operation. In order to solve (12) and facilitate efficient reconstruction, we employ several denoisers/regularizers. For rWF formulation, we experiment with Total Variation (TV) which is known to provide robust image recovery from reduced measurements [24]. Upon application, (12) results in:

$$\boldsymbol{v}^{(k+1)} = \underset{\boldsymbol{v}}{\operatorname{argmin}} \frac{2\lambda}{\mu}\|\boldsymbol{v}\|_{TV} + \|\boldsymbol{v} - \tilde{\boldsymbol{v}}^{(k)}\|_2^2. \quad \text{(rWF-TV)} \tag{16}$$

We also use BM3D denoiser [17] with regularized Wirtinger Flow and refer it as rWF-BM3D. In our work, we have used the MATLAB implementations of Total Variation and BM3D available at [25], [26] respectively for updating $\boldsymbol{v}$. Further, we also employ the recently proposed Deep Image Prior [18] which is an unlearned convolutional neural network (CNN) capable of solving inverse problems in a training-less

setting. Here, contrary to using any explicit regularizer $\mathcal{R}(\boldsymbol{\rho})$, the architecture of a CNN works as an implicit prior with regularization by early-stopping. Algorithm 1 summarizes the PPSAR approach.

IV. RESULTS

For the purpose of comparison, we use similar simulation setting as that of [8]. The transmitter is located at $[15, 15, 0.5]$Km and is assumed to transmit a DVB-T signal having a flat spectrum of bandwidth 8 MHz modulated with a carrier frequency of 760 MHz [27]. This bandwidth provides a range resolution of around 20m. We consider a scene of $[0, 420] \times [0, 420]$m^2 which is discretized into small cells of size 21×21 given the 20m resolution. The SAR platform is assumed to move along a circular trajectory path given by $\boldsymbol{\gamma}(s) = [10\cos(s), 10\sin(s), 6]$Km. Further, in all our simulations, we fix the number of fast-time samples to 50 and vary the number of slow-time samples to change the number of measurements M. Taking 50 samples would amount to taking a fast-time measurement of duration 6.25μsec at each slow-time measurement interval (assuming the uniform sampling rate of 8 MHz). Observe that the aforementioned simulation parameters satisfy the far-field, small scene and start-stop assumption made in Section II. Further, we have used the strategy of choosing λ based on the size of the measurements. In our simulations, we found that this strategy works reasonably well.

We compare the reconstruction obtained using three variations of the proposed rWF approach that use different regularizers/denoisers namely, BM3D, TV and DIP as described in section III. These variations are also compared with the existing vWF, LRMR [7] and Reweighted Wirtinger Flow (RWF) [28] methods. For this, we considered synthetic images taken from [29], two of which are depicted in Fig. 1a and 2a. We vary M by varying the number of slow-time samples. Fig. 1 and Fig. 2 show the reconstruction results of the three regularized techniques with the vWF approach for $M = 500$, 1000 and 6000 phaseless passive SAR measurements. Looking at the results, it can be noticed that the proposed rWF produces better quality reconstructed images even with fewer measurements as compared to vWF. Among rWF approaches, BM3D tends to produce slightly blurry images while TV generates better resolved images. Observe that DIP also promotes image recovery and gives performance comparable to that of TV over a certain range of values of M, however its performance degrades when M is very small.

Fig. 3 provides a quantitative comparison between the vWF, LRMR, RWF and the rWF approaches. From Fig. 3, it can be noticed that rWF-TV provides satisfactory reconstruction from $M = 1000$ onwards and the PSNR gradually improves with the increase in M. Whereas, rWF-BM3D and rWF-DIP require slightly more samples to give satisfactory PSNR values. In the case of vWF and RWF, the improvement in PNSR happens only after a large M. Thus, a significant performance gap between vWF and rWF-TV/DIP can be observed between $M = 1000$ to 4000. Further, it is verified that the LRMR
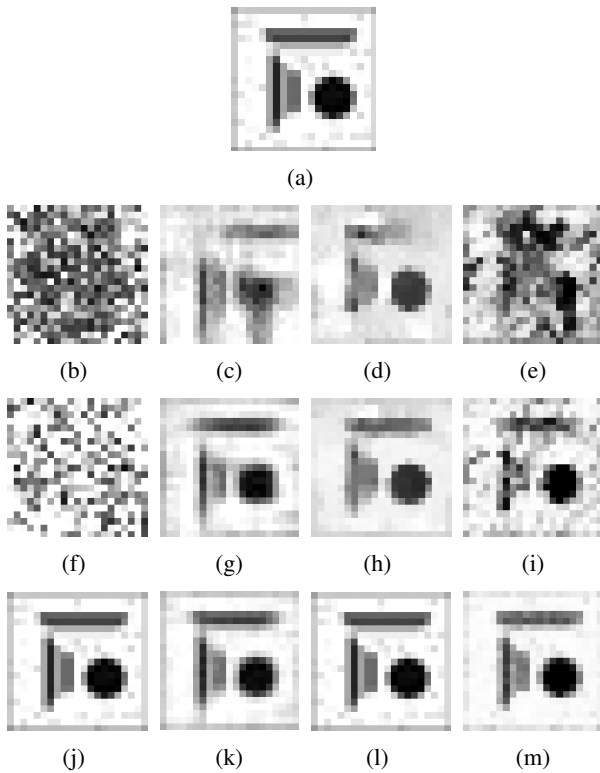
Fig. 1: Reconstruction results for scene 1. (a) Ground truth. $M = 500, 1000$ and 6000 for first, second and third row respectively. Reconstruction results using vWF (first column), rWF-BM3D (second column), rWF-TV (third column) and rWF-DIP (fourth column).
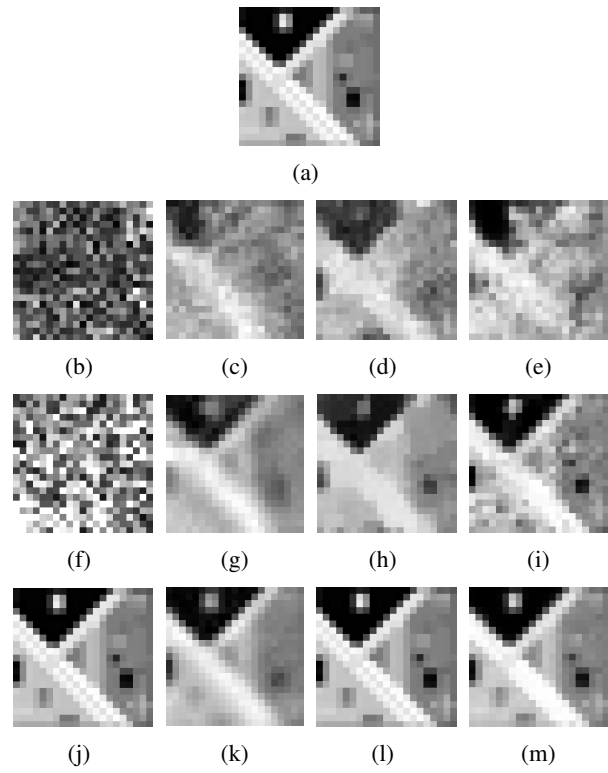

Fig. 2: Reconstruction results for scene 2. (a) Ground truth. $M = 500, 1000$ and 6000 for first, second and third row respectively. Reconstruction results using vWF (first column), rWF-BM3D (second column), rWF-TV (third column) and rWF-DIP (fourth column).

approach performs poorly than the vWF and obviously the rWF approach.

Finally, we compare the robustness of rWF, vWF and RWF for trajectory errors. For fair comparison, we have taken $M = 6000$ since all techniques perform fairly well at this value (see Fig. 3). Fig. 4 shows the plot for PSNR vs trajectory error from which it can noted that while all the approaches fail beyond 5m, the RWF and the proposed rWF approaches show better robustness at lower trajectory errors.

Thus, the above results clearly demonstrate that the proposed rWF provides improved image reconstruction even with fewer phaseless measurements. In particular, rWF-TV provides at least 75% reduction in number of measurements as compared to existing vWF for a similar performance. In addition to providing this significant reduction, the proposed approach also shows more robustness against trajectory errors, hence making it attractive for PPSAR imaging.

V. CONCLUSION

A training-less regularized WF based approach is presented in this paper for PPSAR imaging. The reconstruction is achieved using ADMM iterations by employing state-of-the-art denoising algorithms, namely, Total Variation, BM3D and DIP as priors. Simulations are performed to evaluate the

performance that show a significant reduction in the requisite slow-time samples and robustness against trajectory errors. This reduction ultimately curbs the necessity for large on-board storage and high speed data transfer, thus making the proposed approach attractive for PPSAR imaging.

REFERENCES

[1] I. G. Cumming and F. H. Wong, "Digital processing of synthetic aperture radar data," *Artech house*, vol. 1, no. 3, pp. 108–110, 2005.
[2] C. Jakowatz, D. Wahl, P. Eichel, D. Ghiglia, and P. Thompson, *Spotlight-Mode Synthetic Aperture Radar: A Signal Processing Approach.* Springer US, 2012. [Online]. Available: https://books.google.co.in/books?id=nyEBCAAAQBAJ
[3] F. (ed.) Bovenga, *Synthetic Aperture Radar (SAR) Techniques and Applications.* MDPI, 2020. [Online]. Available: https://books.google.co.in/books?id=kbm1BAAAQBAJ
[4] L. Maslikowski, P. Samczynski, M. Baczyk, P. Krysik, and K. Kulpa, "Passive bistatic sar imaging—challenges and limitations," *IEEE Aerospace and Electronic Systems Magazine*, vol. 29, no. 7, pp. 23–29, 2014.
[5] C. E. Yarman and B. Yazici, "Synthetic aperture hitchhiker imaging," *IEEE transactions on image processing*, vol. 17, no. 11, pp. 2156–2173, 2008.
[6] E. Mason, I.-Y. Son, and B. Yazıcı, "Passive synthetic aperture radar imaging using low-rank matrix recovery methods," *IEEE Journal of Selected Topics in Signal Processing*, vol. 9, no. 8, pp. 1570–1582, 2015.
[7] E. Mason and B. Yazici, "Passive phaseless sar imaging," in *2018 IEEE Radar Conference (RadarConf18).* IEEE, 2018, pp. 0292–0297.

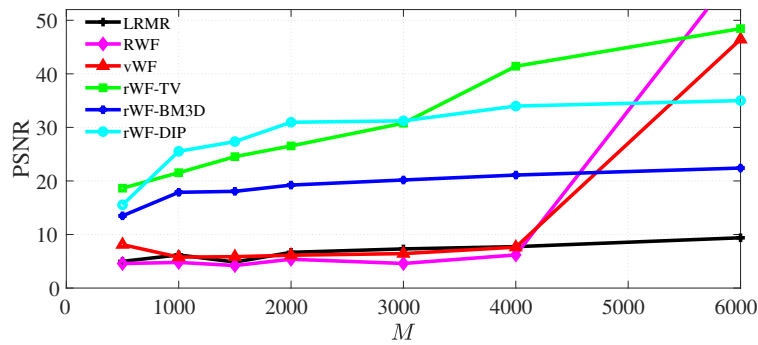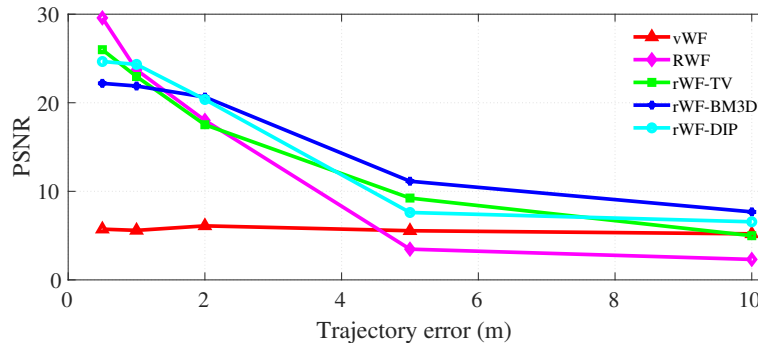Fig. 3: PSNR after reconstruction using LRMR, RWF, vWF and rWF for different values of M.

Fig. 4: PSNR after reconstruction in the presence of trajectory errors in the SAR receiver path.

[8] B. Yonel, E. Mason, and B. Yazici, "Phaseless passive synthetic aperture radar imaging via wirtinger flow," in *2018 52nd Asilomar Conference on Signals, Systems, and Computers*. IEEE, 2018, pp. 1623–1627.

[9] S. Kazemi, B. Yonel, and B. Yazici, "Unrolled wirtinger flow with deep priors for phaseless imaging," *arXiv preprint arXiv:2108.01735*, 2021.

[10] E. J. Candes, X. Li, and M. Soltanolkotabi, "Phase retrieval via wirtinger flow: Theory and algorithms," *IEEE Transactions on Information Theory*, vol. 61, no. 4, pp. 1985–2007, 2015.

[11] Z. Yuan, H. Wang, and Q. Wang, "Phase retrieval via sparse wirtinger flow," *Journal of Computational and Applied Mathematics*, vol. 355, pp. 162–173, 2019.

[12] S. Boyd, N. Parikh, E. Chu, B. Peleato, and J. Eckstein, "Distributed optimization and statistical learning via the alternating direction method of multipliers," *Foundations and Trends® in Machine Learning*, vol. 3, no. 1, pp. 1–122, 2011. [Online]. Available: http://dx.doi.org/10.1561/2200000016

[13] R. Nishihara, L. Lessard, B. Recht, A. Packard, and M. Jordan, "A general analysis of the convergence of admm," in *International Conference on Machine Learning*. PMLR, 2015, pp. 343–352.

[14] Y. Wang, W. Yin, and J. Zeng, "Global convergence of admm in nonconvex nonsmooth optimization," *Journal of Scientific Computing*, vol. 78, no. 1, pp. 29–63, 2019.

[15] S. V. Venkatakrishnan, C. A. Bouman, and B. Wohlberg, "Plug-and-play priors for model based reconstruction," in *2013 IEEE Global Conference on Signal and Information Processing*. IEEE, 2013, pp. 945–948.

[16] L. I. Rudin, S. Osher, and E. Fatemi, "Nonlinear total variation based noise removal algorithms," *Physica D: Nonlinear Phenomena*, vol. 60, no. 1, pp. 259–268, 1992. [Online]. Available: https://www.sciencedirect.com/science/article/pii/016727899290242F

[17] K. Dabov, A. Foi, V. Katkovnik, and K. Egiazarian, "Image denoising by sparse 3-d transform-domain collaborative filtering," *IEEE Transactions on Image Processing*, vol. 16, no. 8, pp. 2080–2095, 2007.

[18] D. Ulyanov, A. Vedaldi, and V. Lempitsky, "Deep image prior," in *Proceedings of the IEEE Conference on Computer Vision and Pattern Recognition (CVPR)*, June 2018.

[19] I.-Y. Son, H. C. Yanik *et al.*, "Doppler synthetic aperture radar interferometry: a novel sar interferometry for height mapping using ultra-narrowband waveforms," *Inverse Problems*, vol. 34, no. 5, p. 055003, 2018.

[20] P. L. Combettes and J.-C. Pesquet, "Proximal splitting methods in signal processing," in *Fixed-point algorithms for inverse problems in science and engineering*. Springer, 2011, pp. 185–212.

[21] M. V. Afonso, J. M. Bioucas-Dias, and M. A. Figueiredo, "An augmented lagrangian approach to the constrained optimization formulation of imaging inverse problems," *IEEE Transactions on Image Processing*, vol. 20, no. 3, pp. 681–695, 2010.

[22] C. Li, W. Yin, H. Jiang, and Y. Zhang, "An efficient augmented lagrangian method with applications to total variation minimization," *Computational Optimization and Applications*, vol. 56, no. 3, pp. 507–530, 2013.

[23] S. H. Chan, X. Wang, and O. A. Elgendy, "Plug-and-play admm for image restoration: Fixed-point convergence and applications," *IEEE Transactions on Computational Imaging*, vol. 3, no. 1, pp. 84–98, 2016.

[24] E. Bostan, U. S. Kamilov, M. Nilchian, and M. Unser, "Sparse stochastic processes and discretization of linear inverse problems," *IEEE TRANSACTIONS ON IMAGE PROCESSING*, vol. 22, no. 7, pp. 2699–2710, 2013.

[25] S. Chan, "deconvtv - fast algorithm for total variation deconvolution," https://www.mathworks.com/matlabcentral/fileexchange/43600-deconvtv-fast-algorithm-for-total-variation-deconvolution, 2021, accessed: October 2, 2021.

[26] Y. Mäkinen *et al.*, "Block-matching and 3d filtering (bm3d) algorithm," https://webpages.tuni.fi/foi/GCF-BM3D/index.html#ref_people, 2021.

[27] J. E. Palmer, H. A. Harms, S. J. Searle, and L. Davis, "Dvb-t passive radar signal processing," *IEEE transactions on Signal Processing*, vol. 61, no. 8, pp. 2116–2126, 2012.

[28] Z. Yuan and H. Wang, "Phase retrieval via reweighted wirtinger flow," *Applied Optics*, vol. 56, no. 9, p. 2418, Mar 2017. [Online]. Available: http://dx.doi.org/10.1364/AO.56.002418

[29] M. B. Alver, A. Saleem, and M. Çetin, "Plug-and-play synthetic aperture radar image formation using deep priors," *IEEE Transactions on Computational Imaging*, vol. 7, pp. 43–57, 2020.